

ON THE STABILITY OF SUPER EARTH ATMOSPHERES

KEVIN HENG^{1,3} AND PUSHKAR KOPPARLA²

Preprint: September 4, 2018

ABSTRACT

We investigate the stability of super Earth atmospheres around M stars using a 7-parameter, analytical framework. We construct stability diagrams in the parameter space of exoplanetary radius versus semi-major axis and elucidate the regions in which the atmospheres are stable against the condensation of their major constituents, out of the gas phase, on their permanent nightside hemispheres. We find that super Earth atmospheres which are nitrogen-dominated (“Earth-like”) occupy a smaller region of allowed parameter space, compared to hydrogen-dominated atmospheres, because of the dual effects of diminished advection and enhanced radiative cooling. Furthermore, some super Earths which reside within the habitable zones of M stars may not possess stable atmospheres, depending on the mean molecular weight and infrared photospheric pressure of their atmospheres. We apply our stability diagrams to GJ 436b and GJ 1214b, and demonstrate that atmospheric compositions with high mean molecular weights are disfavoured if these exoplanets possess solid surfaces and shallow atmospheres. Finally, we construct stability diagrams tailored to the *Kepler* dataset, for G and K stars, and predict that about half of the exoplanet candidates are expected to harbour stable atmospheres if Earth-like conditions are assumed. We include 55 Cancri e and CoRoT-7b in our stability diagram for G stars.

Subject headings: planets and satellites: atmospheres

1. INTRODUCTION

The lower effective temperatures of M stars (or red dwarfs)—which comprise about three-quarters of the stellar population—render the detection of orbiting, close-in, Earth-like exoplanets amenable to both the transit and radial velocity techniques (Charbonneau 2009). The immense interest in hunting for exoplanets around these stars stems from the fact that the habitable zone is located at ~ 0.01 – 0.1 AU, rather than ~ 1 AU, away from these stars (Tarter et al. 2007). A consequence of the close proximity is that the exoplanets are expected to be tidally locked (or spin synchronized),⁴ meaning that they possess permanent dayside and nightside hemispheres. This expectation has led to theoretical concerns that the atmospheres may undergo collapse, because if heat is not redistributed efficiently from the dayside to the nightside it may lead to the dominant chemical species condensing out on the nightside (e.g., Joshi, Haberle & Reynolds 1997; Joshi 2003). For example, Wordsworth et al. (2011) constructed three-dimensional, general circulation models tailored to the study of Gliese 581d and elucidated scenarios for atmospheric stability. Generally, the discovery of close-in super Earths (e.g., Mayor et al. 2009; Charbonneau et al. 2009; Vogt et al. 2010; Anglada-Escudé et al. 2012; Delfosse et al. 2012) has inspired a number of theoretical studies of their possible atmospheres (e.g., Merlis & Schneider 2010; Rogers & Seager 2010; Castan & Menou 2011; Heng, Menou & Phillipps 2011; Heng & Vogt 2011; Heng, Frierson & Phillipps 2011; Pierrehumbert 2011; Valencia et al. 2011; Menou 2012), which either focus on specific case studies or explore a limited range of parameter space.

Specifically, we consider an exoplanet possessing a solid surface which is enveloped by a shallow atmosphere. Whether the surface is made of rock, ice, etc, is unimportant, insofar as it provides a solid, lower boundary for the atmosphere. The atmosphere is assumed to be shallow enough that it may be characterized by advective and radiative time scales which are constant over its entire depth. When the atmosphere is predominantly radiative, heat is thermally re-emitted before it is able to be advected to the permanent nightside. The nightside becomes arbitrarily cold,⁵ thus leading to the condensation of its constituents from the gas to the liquid or solid phases. When this situation occurs, the atmosphere is unlikely to survive for a duration comparable to the stellar age and we term the atmosphere to have “collapsed”. This situation is distinct from the phenomenon of atmospheric escape (e.g., Yelle 2004; Murray-Clay, Chiang & Murray 2009), which concerns the (often slow) vertical flow of material out of the gravitational potential of the exoplanet. When the atmosphere is predominantly advective, the efficient redistribution of heat to the nightside provides a necessary but insufficient condition for the nightside atmosphere to exist in its gaseous form—whether it does depends on the thermodynamics of phase changes of the chemical species being considered, which provides the sufficient condition. If the atmosphere remains in the gas phase, then we term it to be “stable”. In other words, an atmosphere which is sufficiently advective *and* warm will survive for a long time.

In the present paper, the main question we are addressing is: *what is the simplest model one can construct to broadly understand the stability of super Earth atmospheres?* To this end, we introduce an analytical framework which allows for an efficient, broad exploration of parameter space, while keeping the number of free parameters involved to a minimum. The key outcome of our study is the construction of a stability diagram, which allows one to judge if a super Earth atmosphere is likely to survive for a duration comparable to the age of its host star. In §2, we describe our methodology.

¹ ETH Zürich, Institute for Astronomy, Wolfgang-Pauli-Strasse 27, CH-8093, Zürich, Switzerland

² ETH Zürich, Institute for Atmospheric and Climate Science, Universitätsstrasse 16, CH-8092, Zürich, Switzerland

³ Zwicky Prize Fellow

⁴ Strictly speaking, the terms “tidally locked” and “spin synchronized” are only synonymous for an exoplanet residing on a circular orbit (Heller, Leconte & Barnes 2011). We use these terms interchangeably as we do not account for the effects of an eccentric orbit.

⁵ But see discussion of caveats in §4.1.

In §3, we present the basic stability diagram as well as variations of it applied to GJ 436b and GJ 1214b. In §4, we discuss the caveats associated with our model, the implications of our results and also apply our stability diagrams to the *Kepler* dataset of exoplanets and exoplanetary candidates, as well as 55 Cancri e and CoRoT-7b.

2. METHODOLOGY

To efficiently explore a wide range of parameter space, we construct a 7-parameter model with the following inputs:

1. The spatial separation between the exoplanet and its host star (a);
2. The radius of the exoplanet (R);
3. The bulk mass density of the exoplanet (ρ_0);
4. The pressure level associated with the infrared photosphere (P);
5. The mean molecular weight of atmospheric atoms/molecules (μ);
6. The number of degrees of freedom of the atmospheric gas (n_{dof});
7. The Bond albedo of the exoplanetary atmosphere (\mathcal{A}).

These basic parameters yield all of the other secondary parameters. We assume our exoplanets to be spherical, such that the mass is described by $M = 4\pi\rho_0 R^3/3$. The surface gravity is given by $g = 4\pi G\rho_0 R/3$, where G is the universal gravitational constant. In addition, the stellar mass (M_\star), radius (R_\star) and effective temperature (T_\star) need to be specified.

2.1. Stellar Irradiation and Orbital Parameters

The incident flux impinging upon the substellar point is

$$\mathcal{F}_0 = \sigma_{\text{SB}} T_{\text{irr}}^4, \quad (1)$$

where σ_{SB} is the Stefan-Boltzmann constant and the irradiation temperature is

$$T_{\text{irr}} = T_\star \left(\frac{R_\star}{a} \right)^{1/2} (1 - \mathcal{A})^{1/4}. \quad (2)$$

If one adopts parameter values appropriate to Earth (and $\mathcal{A} = 0$), one obtains the solar constant, $\mathcal{F}_0 \approx 1370 \text{ W m}^{-2}$.

Since the assumption of tidal locking is made, the orbital and rotational frequency are equal and given by (assuming that $M_\star \gg M$)

$$\Omega = \left(\frac{GM_\star}{a^3} \right)^{1/2}. \quad (3)$$

It is thus clear that T_{irr} (or \mathcal{F}_0) and Ω need to be varied self-consistently as one changes a .

2.2. Thermodynamics

The mean molecular mass $m = \mu m_{\text{H}}$ (with m_{H} denoting the mass of a hydrogen atom) and the number of degrees of freedom of the atmospheric gas n_{dof} collectively describe the thermodynamics and are manifested macroscopically via the adiabatic gas index,

$$\Gamma = 1 + \frac{2}{n_{\text{dof}}}, \quad (4)$$

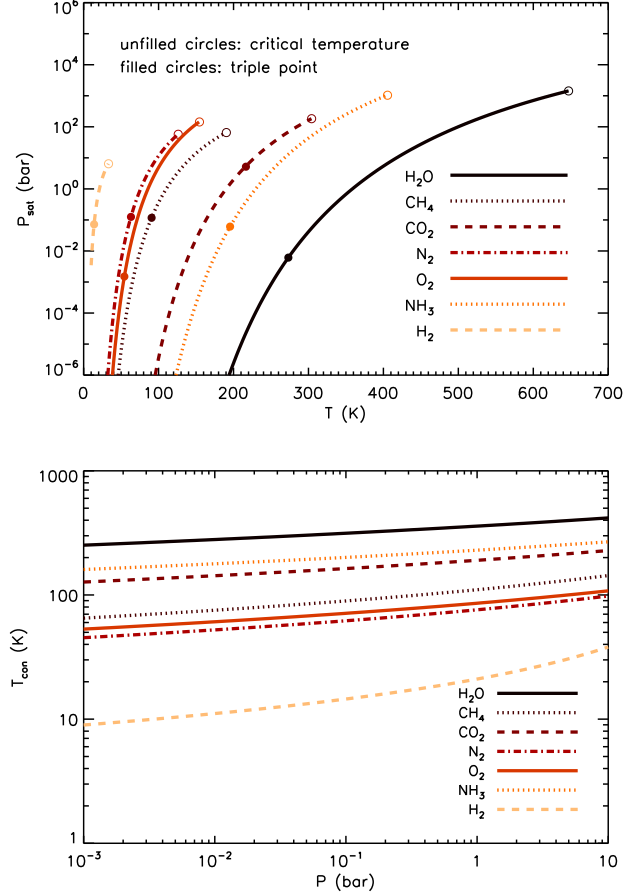


FIG. 1.— Top panel: approximate phase diagrams of various molecular species as computed using the Clausius-Clapeyron equation. At a given temperature, chemical species existing at a pressure above their respective saturation pressure curves are in the liquid or solid phase. Bottom panel: condensation temperature as a function of pressure. At a given pressure, chemical species existing at a temperature above T_{con} are in the gas phase.

as well as the adiabatic coefficient (Pierrehumbert 2010),

$$\kappa = \frac{2}{2 + n_{\text{dof}}} = \frac{\mathcal{R}}{c_P}, \quad (5)$$

where $\mathcal{R} = \mathcal{R}^*/\mu$ is the specific gas constant and $\mathcal{R}^* = 8314.5 \text{ J K}^{-1} \text{ kg}^{-1}$ is the universal gas constant. The sound speed is $c_s = (\Gamma k_B T_{\text{irr}}/m)^{1/2}$, where k_B is the Boltzmann constant. Furthermore, the specific heat capacity,

$$c_P = \frac{(2 + n_{\text{dof}}) \mathcal{R}^*}{2\mu}, \quad (6)$$

is used in evaluating the radiative time scale t_{rad} .

As an example, atmospheres dominated by molecular hydrogen have $\mu = 2$ and $n_{\text{dof}} = 5$, such that $\Gamma = 7/5$, $\kappa = 2/7$ and $\mathcal{R} = 4157.25 \text{ J K}^{-1} \text{ kg}^{-1}$. Dry, terrestrial air (dominated by nitrogen and oxygen) has a mean molecular weight of $\mu \approx 28.97$, such that $\mathcal{R} \approx 287 \text{ J K}^{-1} \text{ kg}^{-1}$. As a further example, we note that the model with $\mu \approx 17$ from Menou (2012) is termed “Water”, with relevance to a possible subclass of H_2O -dominated super Earths known as “water worlds” (Charbonneau et al. 2009; Rogers & Seager 2010; Bean et al. 2011). In practice, the effective number of degrees of freedom n_{dof} is not an integer (e.g., see Table 2.1, pg. 92, of Pierrehumbert 2010). For example, CO_2 has $n_{\text{dof}} \approx 6.8$, O_2 has $n_{\text{dof}} \approx 5.1$ and H_2 has $n_{\text{dof}} \approx 5.2$. For simplicity

TABLE 1
TABLE OF THERMODYNAMIC QUANTITIES FOR VARIOUS MOLECULAR SPECIES

Species	μ	L_{avg} (J kg $^{-1}$)	$T_{\text{con},0}$ (K)	T_{crit} (K)	$P_{\text{sat},0}$ (bar)	P_{crit} (bar)
H ₂ O	18	2.7×10^6	5845	647.1	1.2×10^7	221
CH ₄	16	5.7×10^5	1097	190.44	2.1×10^4	45.96
CO ₂	44	5.0×10^5	2646	304.2	1.1×10^6	73.825
N ₂	28	2.3×10^5	775	126.2	2.7×10^4	34.0
O ₂	32	2.5×10^5	962	154.54	7.4×10^4	50.43
NH ₃	17	1.8×10^6	3680	405.5	9.2×10^6	112.8
H ₂	2	4.5×10^5	108	33.2	1.7×10^2	12.98

and to not obscure the salient physics of the model, we adopt $n_{\text{dof}} = 5$.

To determine if a given chemical species exists in the gas or liquid/solid phase, one needs to have knowledge of the saturation pressure P_{sat} . If the atmospheric pressure exceeds the saturation pressure, then the molecule (or atom) will condense out of the gas phase and into the liquid/solid phase. The dependence of P_{sat} on the temperature T is governed by the Clausius-Clapeyron equation (e.g., §2.6 of Pierrehumbert 2010),

$$\frac{dP_{\text{sat}}}{dT} = \frac{P_{\text{sat}} T_{\text{con},0}}{T^2}, \quad (7)$$

where $T_{\text{con},0} \equiv L_{\text{avg}}/\mathcal{R}$ is the characteristic condensation temperature. Depending on whether one is describing the gas-liquid or gas-solid phase change, one needs to specify the latent heat of condensation or sublimation, respectively. For most gases, the difference between these two latent heats is small (≈ 5 –10%); an exception is CO₂, where the difference is about 33%. For simplicity, we adopt the average value of these two latent heats (L_{avg}) using Table 2.1 of Pierrehumbert (2010). Furthermore, the value of L_{avg} remains fairly constant unless $T \gg T_{\text{con},0}$. Thus, the Clausius-Clapeyron equation can be integrated to obtain

$$P_{\text{sat}} = P_{\text{sat},0} \exp\left(-\frac{T_{\text{con},0}}{T}\right), \quad (8)$$

where the normalization constant $P_{\text{sat},0}$ is computed using the pressure and temperature associated with the triple point of a given chemical species. In Table 1, we list L_{avg} , $T_{\text{con},0}$ and $P_{\text{sat},0}$ for several molecular species. The top panel of Figure 1 shows the corresponding (and approximate) phase diagrams, which include the triple points associated with each species.

Our use of the saturation pressure curves is valid as long as one is not above the temperature T_{crit} and the pressure P_{crit} associated with the critical point. In this regime, the atmosphere exists as a supercritical fluid where distinct liquid and gas phases do not exist. If the atmosphere is above the critical temperature but below the critical pressure, then it exists as a gas. Since we typically have $P_{\text{crit}} > 10$ bar (which is larger than the pressures we consider), we assume our model atmospheres to be gaseous when $T > T_{\text{crit}}$.

At the infrared photosphere (located at a pressure P), the atmosphere remains in gaseous form if $P < P_{\text{sat}}$, which may be recast as the condition $T > T_{\text{con}}$ where

$$T_{\text{con}} \equiv \frac{T_{\text{con},0}}{\ln(P_{\text{sat},0}/P)} \quad (9)$$

is the condensation temperature. The logarithmic factor $\ln(P_{\text{sat},0}/P)$ implies that T_{con} has a somewhat gentle dependence on chemical composition. In the bottom panel of Figure 1, we see that $T_{\text{con}} \sim 100$ K. An exception is molecular

hydrogen for which $T_{\text{con}} \sim 10$ K over a wide range of photospheric pressures. Generally, it becomes less difficult to condense out a given chemical species as the pressure increases.

2.3. Infrared Photospheric Pressure

We assume a thin atmosphere with a Bond albedo \mathcal{A} , such that a fraction $(1 - \mathcal{A})$ of the stellar flux reaches the surface, which resides at a pressure P_0 . The starlight is absorbed and re-emitted in the infrared at a photospheric pressure $P < P_0$. Furthermore, we assume $P \sim P_0$ such that we may apply a shallow water model to represent the entire atmosphere between P and P_0 . The atmosphere is also thin in the sense that the radiative time scale t_{rad} is assumed to be approximately constant throughout, at least near the substellar point. We regard P as a free parameter which characterizes the thickness of the atmosphere.⁶

While we model our atmospheres as consisting purely of molecular hydrogen or nitrogen in our stability diagrams, the assumption is that they also contain minor amounts of other chemical species which absorb strongly in the infrared but constitute an insignificant fraction of the total mass of the atmosphere. This enables us to define a “mean gas” with a mean molecular weight and to compute quantities such as c_P . We further assume that these trace constituents are scarce enough that their partial pressures are miniscule, such that they always remain in the gas phase. In this case, atmospheric stability is dictated by the main constituent (i.e., H₂ or N₂) existing in the gaseous regime of the phase diagram. The typical collisional time between the major and minor constituents of the atmosphere is assumed to be the shortest time scale in the system, such that the atmosphere may be modeled as a single fluid. We neglect any effects associated with clouds or hazes (e.g., see Heng et al. 2012).

2.4. Hydrodynamic Shallow Water Model

We utilize the linear, analytical, steady-state, two-dimensional version of the shallow water model of Showman & Polvani (2011) to model the photosphere of a super Earth. (See also Showman & Polvani 2010.) The shallow water system has traditionally been used to model both the terrestrial atmosphere and ocean (Matsuno 1966; Longuet-Higgins 1968; Gill 1980), but has been generalized by Showman & Polvani (2011) to include radiative forcing and drag within the context of spin-synchronized exoplanets. (See also Heng & Spitkovsky 2009 and references therein.) Several adjustments are required to mimic the variation of var-

⁶ This situation is distinct from that of hot Jupiters, where one parametrizes the optical depths by two broadband opacities (Heng et al. 2012). The radiative time scale is generally not constant for hot Jupiters and varies with depth. The variation of shortwave scattering (i.e., albedo) shifts the photon deposition depth to different heights, resulting in varying degrees of heat redistribution between the dayside and nightside hemispheres (Heng 2012).

ious atmospheric quantities with the strength of stellar irradiation.

Firstly, we need to relate the mean shallow water height H to a characteristic height in the atmosphere, which we identify as the pressure scale height,

$$H = \frac{k_B T_{\text{irr}}}{mg}. \quad (10)$$

Secondly, we set the thermal forcing term S_0 (which has physical units of cm s^{-1}) to be H/t_0 , where $t_0 = (gH)^{-1/4} \beta^{-1/2}$ is the characteristic time scale used to non-dimensionalize the forcing and $\beta = 2\Omega/R$, and also adopt a zonal wave number of 0.5. In other words, the dimensionless forcing is set to be unity. The third ingredient is the radiative time scale (Goody & Yung 1989), which is the ratio of the thermal energy content per unit area ($c_P T_{\text{irr}} \tilde{m}$ where $\tilde{m} = P/g$ is the column mass in hydrostatic equilibrium) to the flux \mathcal{F}_0 ,

$$t_{\text{rad}} = \frac{c_P P}{\sigma_{\text{SB}} g T_{\text{irr}}^3}, \quad (11)$$

which enters into the momentum equations via a radiative drag term ($-\vec{v}/t_{\text{rad}}$).

The fourth—and most uncertain—ingredient is the hydrodynamic drag time scale, which we set to be the rotational/orbital period,

$$t_{\text{drag}} = \frac{2\pi}{\Omega}. \quad (12)$$

On Earth, the source of hydrodynamic drag originates from the boundary layer (Garratt 1994), which is the transition region from a “no slip” to a “free slip” condition between the atmosphere and the terrestrial surface. In the Held-Suarez benchmark test for Earth, the time scale for Rayleigh drag is set to be one Earth day (Held & Suarez 1994). Our simple assumption for t_{drag} is plausible and commensurate with the fact that the true source of drag in super Earth atmospheres remains to be identified. Even the simplest implementation of a boundary layer scheme for Earth (Troen & Mahrt 1986; Frierson, Held & Zurita-Gotor 2006) requires the specification of four additional parameters, which is currently unjustified given the dearth of astronomical information on this issue.

2.5. Basic Trends with Strength of Stellar Irradiation

To assess the efficiency of heat redistribution from the dayside to the nightside hemisphere of a tidally-locked super Earth, one needs to compare the radiative to the advective time scale (Showman & Guillot 2002). Perna, Heng & Pont (2012) have shown using three-dimensional simulations of atmospheric circulation—albeit in the context of hot Jupiters—that a reasonable approach to computing the advective time scale is to evaluate

$$t_{\text{adv}} \sim \frac{R}{u_{\text{max}}}, \quad (13)$$

where $u_{\text{max}} \equiv \max\{u\}$ and u is the zonal wind speed.

While we do not expect the shallow water model of Showman & Polvani (2011) to reproduce all of the trends obtained from the three-dimensional simulations, we do expect u_{max} to generally increase with T_{irr} when hydrodynamic drag is insignificant. The right panel of Figure 2 confirms this expectation for $a \gtrsim 0.1$ AU, a basic trend which is supported by the results obtained from three-dimensional simulations of

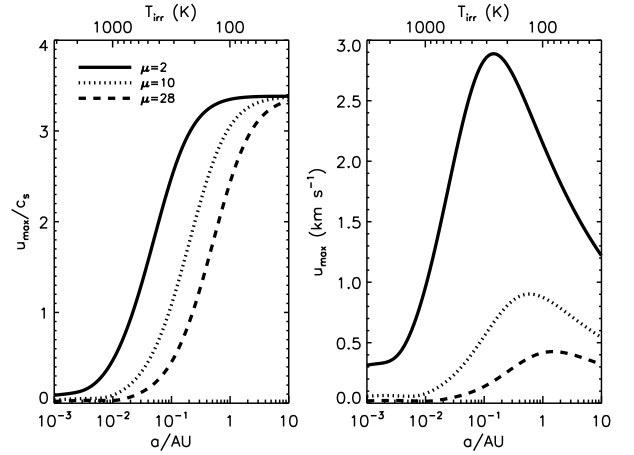


FIG. 2.— Variation of the maximum zonal wind speed, non-dimensionalized (left panel) and in physical units (right panel), with a (or T_{irr}), computed using the shallow water model of Showman & Polvani (2011) which is specialized to tidally-locked exoplanets. For illustration, we adopt $M_* = 0.184 M_{\odot}$, $R_* = 0.203 R_{\odot}$ and $T_* = 3240$ K (appropriate to a M3.5 star) as well as $P = 0.1$ bar and $\mathcal{A} = 0$. Shown also are the curves for different values of the mean molecular weight μ .

atmospheric circulation (e.g., Perna, Heng & Pont 2012). At $a \lesssim 0.1$ AU, the hydrodynamic drag condition we have imposed to mimic the effects of the boundary layer sets in and reverses the trend. We have checked that if t_{drag} is kept constant (and at a large value), then u_{max} increases monotonically with decreasing a . The left panel of Figure 2, which shows the maximum zonal wind speed normalized by the sound speed, illustrates the effects of hydrodynamic drag more succinctly.

The model also predicts that u_{max} decreases when the mean molecular weight increases, because a larger value of μ corresponds to stronger radiative forcing (i.e., shorter t_{rad}). Such a trend with μ is consistent with the simulated results of Menou (2012), who—by examining models for GJ 1214b with $\mu \approx 2, 3$ and 17—found that a higher value of μ leads to a higher ratio of dayside to nightside photospheric flux, implying that heat redistribution becomes less efficient as μ increases. We have checked that the qualitative trends in our stability diagrams are similar whether we adopt $t_{\text{drag}} = 2\pi/\Omega$ or as a constant, arbitrary value, although the quantitative results do differ.

Three-dimensional numerical solutions of the (more general) hydrodynamic primitive equations (e.g., Vallis 2006) predict $\sim 1\text{--}2$ km s^{-1} zonal flows, which are mildly supersonic, to be present in hypothetical super Earth atmospheres tailored to the study of GJ 1214b (Menou 2012). Our estimates for the maximum zonal wind speed are broadly consistent with these calculations. Supersonic flows are permitted in shallow water models (e.g., Antuono 2010), and the assumption of vertical hydrostatic equilibrium does not affect the speed of the horizontally propagating sound waves in general (MacDonald, Lee & Xie 2000).

2.6. Inefficiency of Thermal Conduction

We assume that the rocky cores of our model super Earths do not efficiently conduct enough heat from the irradiated dayside hemisphere to the cold nightside hemisphere to prevent atmospheric collapse. We will now demonstrate that this is a plausible assumption.

In one dimension, the conduction equation reads

$$\frac{\partial T}{\partial t} = \alpha_0 \frac{\partial^2 T}{\partial x^2}, \quad (14)$$

where T denotes the temperature, t the time, x the spatial coordinate and

$$\alpha_0 = \frac{k_{\text{cond}}}{\rho_0 c_{P_0}} \quad (15)$$

is the thermal diffusivity of the material of the rocky core. Here, c_{P_0} denotes the specific heat capacity, at constant pressure, of the rocky core (and not the atmosphere). Assuming that $T = T(x, t) = T_x(x)T_t(t)$ is a separable function of x and t yields

$$\frac{dT_t}{dt} = -C\alpha_0 T_t, \quad (16)$$

which has the solution

$$T_t = T_{t_0} \exp(-C\alpha_0 t), \quad (17)$$

where $T_{t_0} \equiv T_t(t = 0)$ and $-C$ is the separation constant. We identify $C = 1/R^2$, such that the characteristic thermal conduction time scale is

$$\begin{aligned} t_{\text{cond}} &= \frac{\rho_0 c_{P_0} R^2}{k_{\text{cond}}} \\ &\approx 4 \times 10^7 \text{ yr} \left(\frac{\rho_0}{3 \text{ g cm}^{-3}} \frac{c_{P_0}}{10^7 \text{ erg K}^{-1} \text{ g}^{-1}} \right) \\ &\quad \times \left(\frac{R}{R_{\oplus}} \right)^2 \left(\frac{k_{\text{cond}}}{10^{10} \text{ erg K}^{-1} \text{ s}^{-1}} \right)^{-1}. \end{aligned} \quad (18)$$

Rocky material is expected to have a thermal conductivity of $k_{\text{cond}} \sim 1 \text{ W mK}^{-1} = 10^{10} \text{ erg K}^{-1} \text{ s}^{-1}$ and a specific heat capacity of $c_{P_0} \sim 10^7 \text{ erg K}^{-1} \text{ g}^{-1}$. Demanding that the radiative cooling time is less than the thermal conduction time yields the condition

$$\begin{aligned} T &> \left(\frac{k_{\text{cond}}}{\sigma_{\text{SB}} R} \right)^{1/3} \\ &\approx 65 \text{ K} \left(\frac{k_{\text{cond}}}{10^{10} \text{ erg K}^{-1} \text{ s}^{-1}} \right)^{1/3} \left(\frac{R}{R_{\oplus}} \right)^{-1/3}. \end{aligned} \quad (19)$$

The condition in equation (19) implies that as long as the rocky surfaces of close-in super Earths are heated to $\gtrsim 100 \text{ K}$, thermal conductivity will not operate rapidly enough to heat the cold nightside hemisphere. The possibility of significant geothermal heating from the core is not considered in our models and remains a topic for future investigation.

3. STABILITY DIAGRAMS

3.1. Conditions Related to Advection & Radiation

Since the atmosphere is predominantly forced by stellar irradiation, the main effect is the competition between advection and radiative cooling. A plausible, necessary condition for atmospheric stability is $t_{\text{adv}} < t_{\text{rad}}$, which yields

$$R < \left(\frac{c_P u_{\text{max}} P}{\sigma_{\text{SB}} g} \right) T_{\star}^{-3} R_{\star}^{-3/2} (1 - \mathcal{A})^{-3/4} a^{3/2}. \quad (20)$$

The maximum zonal wind speed, u_{max} , is obtained from our shallow water model (see §2.4). A reasonable approximation to the condition in equation (20) is to set $u_{\text{max}} = c_s$, which yields

$$\begin{aligned} R &< \left(\frac{\Gamma k_{\text{B}}}{m} \right)^{1/4} \left(\frac{3c_P P}{4\pi G \rho_0 \sigma_{\text{SB}}} \right)^{1/2} \\ &\quad \times T_{\star}^{-5/4} R_{\star}^{-5/8} (1 - \mathcal{A})^{-5/16} a^{5/8}. \end{aligned} \quad (21)$$

Since free gravity waves have a speed $\sim c_s$, the condition in equation (21) may also be interpreted as a constraint on heat redistribution mediated by free gravity waves.

We have made the assumption that if convective instability is triggered, it leads to the redistribution of heat primarily in the vertical and meridional directions (and not in the zonal direction), which is corroborated by three-dimensional simulations of atmospheric circulation for tidally-locked, Earth-like exoplanets (Joshi 2003; Merlis & Schneider 2010; Heng & Vogt 2011; Heng, Frierson & Phillipps 2011).

3.2. Conditions Related to Thermodynamics of Phase Changes

If advection manages to redistribute heat across the entire exoplanetary atmosphere, then it may be described by an equilibrium temperature $T_{\text{eq}} = T_{\text{irr}}/\sqrt{2}$. Thus, we may identify the temperature in equation (8) as $T = T_{\text{eq}}$.

Generally, the atmosphere remains in the gas phase if

$$a < \max \{a_{\text{con}}, a_{\text{crit}}\}. \quad (22)$$

The condensation distance is given by

$$a_{\text{con}} \equiv \frac{R_{\star}}{2} \left(\frac{T_{\star}}{T_{\text{con},0}} \right)^2 (1 - \mathcal{A})^{1/2} \left[\ln \left(\frac{P_{\text{sat},0}}{P} \right) \right]^2, \quad (23)$$

while the critical distance is given by

$$a_{\text{crit}} \equiv \frac{R_{\star}}{2} \left(\frac{T_{\star}}{T_{\text{crit}}} \right)^2 (1 - \mathcal{A})^{1/2}. \quad (24)$$

Typically, we have $a_{\text{crit}} < a_{\text{con}}$ because $T_{\text{crit}} > T_{\text{con}}$.

In other words, an atmosphere consisting of a single chemical species (described by $T_{\text{con},0}$ and $P_{\text{sat},0}$) will remain stable if the exoplanet is located sufficiently close to its host star, such that the atmospheric molecule (or atom) remains in the gas phase. If the atmosphere contains several chemical species, then P refers to the partial pressure of a given species. In the present study, we consider only atmospheres consisting predominantly of H_2 and N_2 .

3.3. Conditions Related to Orbital Circularization & Spin Synchronization

Our application of the Showman & Polvani (2011) shallow water model breaks down—and the concerns about atmospheric stability are alleviated or even obviated—if the exoplanet is not spin-synchronized, but still (approximately) applies if it resides on a mildly eccentric orbit.⁷ (See Laughlin et al. 2009 for an illustration of the effects of stellar irradiation on the atmosphere of an exoplanet residing on a highly eccentric, but spin-synchronized, orbit. See also Heller, Leconte & Barnes 2011.) The time scale associated with spin synchronization is (Bodenheimer, Lin & Mardling 2001)

$$t_{\text{syn}} = \frac{8Q}{45\Omega} \left(\frac{\omega}{\Omega} \right) \left(\frac{M}{M_{\star}} \right) \left(\frac{a}{R} \right)^3, \quad (25)$$

where ω is the *rotational* frequency of an exoplanet which is not initially spin-synchronized. The time scale associated with the circularization of the orbit is (Goldreich & Soter 1966)

$$t_{\text{circ}} = \frac{4Q}{63\Omega} \left(\frac{M}{M_{\star}} \right) \left(\frac{a}{R} \right)^5. \quad (26)$$

⁷ We will see later that the $t_{\text{adv}} = t_{\text{rad}}$ and the $t_{\text{circ}} = t_{\star}$ lines typically do not intersect.

In both equations (25) and (26), the tidal quality factor is $Q = 2\pi E_{\text{peak}}/\Delta E$, where E_{peak} is the peak tidal energy stored and ΔE is the amount of energy dissipated per forcing cycle (Knopoff 1964; Goldreich & Soter 1966; Bodenheimer, Lin & Mardling 2001). Following Knopoff (1964) and Goldreich & Soter (1966), we adopt $Q = 10\text{--}100$ for rocky exoplanets. Spin synchronization generally occurs faster than orbital circularization, unless

$$a < R\sqrt{\frac{14}{5}}\left(\frac{\omega}{\Omega}\right). \quad (27)$$

If $\omega/\Omega = 100$, then the numerical coefficient in equation (27) is about 17. This condition appears unlikely to be satisfied. Demanding that $t_{\text{syn}} < t_*$ and $t_{\text{circ}} < t_*$ yield a pair of respective conditions:

$$\begin{aligned} a &< \left(\frac{135t_*}{32\pi Q\rho_0}\right)^{2/9} \left(\frac{\Omega}{\omega}\right)^{2/9} G^{1/9} M_*^{1/3}, \\ R &> \left(\frac{16\pi Q\rho_0}{189t_*}\right)^{1/2} G^{-1/4} M_*^{-3/4} a^{13/4}. \end{aligned} \quad (28)$$

A caveat is that if the exoplanet ends up in 1 : N tidal resonances where $N > 1$, then this tends to homogenize the zonal temperature differences, thus further alleviating concerns about atmospheric collapse (Wordsworth et al. 2011).

3.4. Other Conditions

In order to retain its atmosphere, a super Earth needs to possess a radius which is smaller than its Hill sphere $R_{\text{H}} = a(M/3M_*)^{1/3}$, which implies that

$$a > \left(\frac{9M_*}{4\pi\rho_0}\right)^{1/3}. \quad (29)$$

The thermal speed ($\sim c_s$) of the atmospheric gas also needs to not exceed the escape speed of the exoplanet, $v_{\text{esc}} = (2GM/R)^{1/2}$,

$$R > \left(\frac{3\Gamma k_{\text{B}}}{8\pi G\rho_0 m}\right)^{2/3} T_*^{2/3} (1 - \mathcal{A})^{1/6} a^{-1/3}. \quad (30)$$

Equation (30) may be regarded as being liberal, as atmospheric escape (e.g., Yelle 2004; Murray-Clay, Chiang & Murray 2009) will still occur when $v_{\text{esc}} > c_s$. We do not expect the lower limit in equation (30) to be revised upward by more than an order of magnitude if atmospheric escape is properly accounted for (and if it occurs at a sufficiently high rate to be relevant over the stellar age).

The habitable zone, which is the range of distances from a star where an Earth-like exoplanet can permanently harbor liquid water, may be described by fitting formulae based on one-dimensional radiative-convective calculations (Selsis et al. 2007):

$$\begin{aligned} a_{\text{in}} &= 1 \text{ AU} \left(a_1 - a_2 \tilde{T}_* - a_3 \tilde{T}_*^2 \right) \left(\frac{\mathcal{L}_*}{\mathcal{L}_\odot} \right)^{1/2}, \\ a_{\text{out}} &= 1 \text{ AU} \left(a_4 - a_5 \tilde{T}_* - a_6 \tilde{T}_*^2 \right) \left(\frac{\mathcal{L}_*}{\mathcal{L}_\odot} \right)^{1/2}, \end{aligned} \quad (31)$$

where $\tilde{T}_* \equiv T_* - 5700 \text{ K}$, $\mathcal{L}_* = 4\pi R_*^2 \sigma_{\text{SB}} T_*^4$ and $\mathcal{L}_\odot = 3.839 \times 10^{33} \text{ erg s}^{-1}$. The fitting coefficients are $a_1 = 0.84$, $a_2 = 2.7619 \times 10^{-5} \text{ K}^{-1}$, $a_3 = 3.8095 \times 10^{-9} \text{ K}^{-2}$,

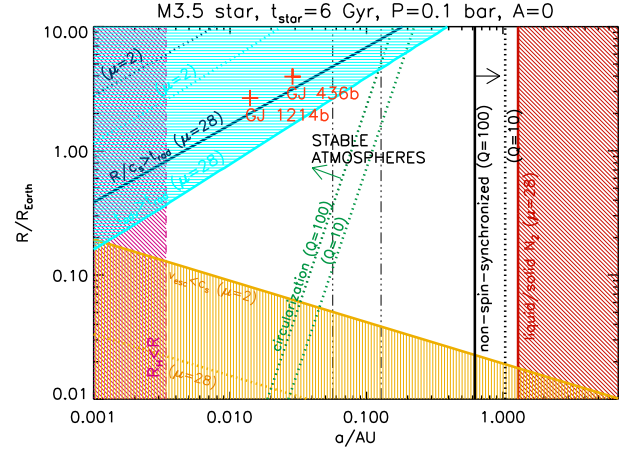


FIG. 3.— Basic stability diagram in the parameter space of exoplanetary radius (R) versus the spatial separation between the exoplanet and its host star (a). The hatched regions mark the regimes in which the atmosphere is unstable. The pressure associated with the infrared photosphere is set to be $P = 0.1$ bar, while the Bond albedo is $\mathcal{A} = 0$. The boundaries of the habitable zone are marked by the pair of vertical, triple-dot-dash lines. For H_2 , we have $a_{\text{con}} \approx 24 \text{ AU}$, and thus it is not shown in the diagram.

$a_4 = 1.67$, $a_5 = 1.3786 \times 10^{-4} \text{ K}^{-1}$ and $a_6 = 1.4286 \times 10^{-9} \text{ K}^{-2}$. The quantities a_{in} and a_{out} represent the inner and outer boundaries, respectively. For simplicity, we have adopted a cloud-free description of the habitable zone; in such a scenario, the habitable zone for the Solar System extends from about 0.84–1.67 AU.

3.5. Basic Stability Diagram

Figure 3 shows the basic stability diagram for super Earth atmospheres in the parameter space of R versus a . For the condition $t_{\text{syn}} < t_*$, we have used $\omega/\Omega = 100$ merely as an illustration. As expected, the condition $R/c_s < t_{\text{rad}}$ is less constraining than $t_{\text{adv}} < t_{\text{rad}}$ across all of the considered values of R , a and μ ; reassuringly, both conditions produce similar qualitative trends. The condition $R_{\text{H}} > R$ is overwhelmed by both the $t_{\text{adv}} < t_{\text{rad}}$ and $v_{\text{esc}} > c_s$ conditions. A key feature of Figure 3 is that atmospheres with lower mean molecular weights (μ) tend to occupy a larger allowed region of parameter space.

We include in Figure 3 the measured values of R and a for GJ 436b and GJ 1214b. For GJ 436b, we use the values of $R \approx 3.96R_{\oplus}$ and $a \approx 0.0287 \text{ AU}$ as reported by Knutson et al. (2011). For GJ 1214b, we use the values of $R \approx 2.66R_{\oplus}$ and $a \approx 0.014 \text{ AU}$ as reported by Carter et al. (2011). Since both GJ 436b and GJ 1214b have a bulk density of $\rho_0 \approx 2 \text{ g cm}^{-3}$, we adopt this value. We adopt stellar parameters appropriate to a M3.5 star ($M_* = 0.184M_{\odot}$, $R_* = 0.203R_{\odot}$, $T_* = 3240 \text{ K}$) as a compromise between the M2.5 and M4.5 host stars of GJ 436b and GJ 1214b, respectively (Ehrenreich & Désert 2011); we will refine these parameter values later in §3.6. We also use $t_* = 6 \text{ Gyr}$ to be consistent with the reported ages of the host stars.

Another key feature of Figure 3 is that some super Earths ($R \gtrsim R_{\oplus}$) residing in the habitable zone (equation [31]), with nitrogen-dominated (“Earth-like”) atmospheres ($\mu = 28$), do not possess stable atmospheres. Certainly, this statement depends on the assumed value of the infrared photospheric pressure P . Although we do not explicitly include it in our stability diagram, we have repeated the exercise for oxygen-dominated atmospheres ($\mu = 32$) and find that the conclusions associated with them are similar to those for

nitrogen-dominated atmospheres. Thus, it is reasonable to term nitrogen-dominated atmospheres as being “Earth-like”.

Kite, Gaidos & Manga (2011) have identified a pair of climate instabilities, related to weathering, which are suppressed for atmospheres with high radiative efficiencies (i.e., short t_{rad}). Specifically, the enhanced substellar weathering instability (ESWI) operates when advection is efficient enough to counteract the increase in temperature near the substellar point, which decreases the rate of weathering. The supply of greenhouse gases (via outgassing) now outweighs its removal, implying that a runaway greenhouse effect may be triggered. Thus, ESWI is activated when advection is efficient, but it acts on geological, rather than dynamical, time scales. This has the implication that even if irradiation is strong enough to suppress advection and the ESWI, atmospheric collapse will still occur. At face value, our results are orthogonal to those of Kite, Gaidos & Manga (2011), implying that super Earths which manage to overcome the ESWI need to also possess sufficiently advective atmospheres to avoid collapse. Future work will elucidate the restricted parameter space in which both effects are precluded.

3.6. Stability Diagrams Applied to GJ 436b and GJ 1214b

To construct stability diagrams in the parameter space of μ versus P , we rewrite the condition in equation (20):

$$\mu < \left[\frac{(2 + n_{\text{dof}}) \mathcal{R}^* u_{\text{max}} P}{2\sigma_{\text{SB}} g R} \right] T_*^{-3} R_*^{-3/2} (1 - \mathcal{A})^{-3/4} a^{3/2}. \quad (32)$$

For GJ 436, we use $M_* = 0.45M_{\odot}$, $R_* = 0.46R_{\odot}$ and $T_* = 3585$ K (Ehrenreich & Désert 2011). For GJ 1214, we use $M_* = 0.15M_{\odot}$, $R_* = 0.21R_{\odot}$ and $T_* = 3026$ K (Ehrenreich & Désert 2011). The surface gravities of GJ 436b and GJ 1214b are approximately 13.0 and 9.0 m s⁻², respectively.

Figure 4 shows the stability diagrams as functions of μ and P , specialized to GJ 436b and GJ 1214b. In general, atmospheres with high mean molecular weights (μ) and low P values are unlikely to be stable due to the violation of the $t_{\text{adv}} < t_{\text{rad}}$ condition.

The *Spitzer* transmission spectrum of GJ 436b reveals variations indicative of spectral absorption features associated with carbon monoxide and methane (Knutson et al. 2011). Our stability diagram for GJ 436b allows for a stable atmosphere with $\mu \sim 10$ if the photosphere resides at $P \gtrsim 1$ bar and $\mathcal{A} = 0$. Non-zero values of the Bond albedo allow for higher values of μ . Inferences about the atmospheric composition of GJ 1214b remain controversial (Rogers & Seager 2010; Bean et al. 2011; Croll et al. 2011; Désert et al. 2011; de Mooij et al. 2012; Miller-Ricci Kempton, Zahnle & Fortney 2012), including the possibility that a reduced value of the radius—which may obtain from an updated estimate of the distance to GJ 1214 via improved parallax measurements—is consistent with an atmosphere-less exoplanet. Detecting or ruling out the presence of a Rayleigh scattering slope in the spectrum at shorter wavelengths is a valuable atmospheric diagnostic for μ (de Mooij et al. 2012).

4. DISCUSSION

The theory of (exo)planet formation remains fraught with uncertainties. Therefore, an attempt to construct a formation model for super Earth atmospheres—which are probably secondary (i.e., due to outgassing) and unlikely to reflect the elemental compositions of the primordial nebulae from which

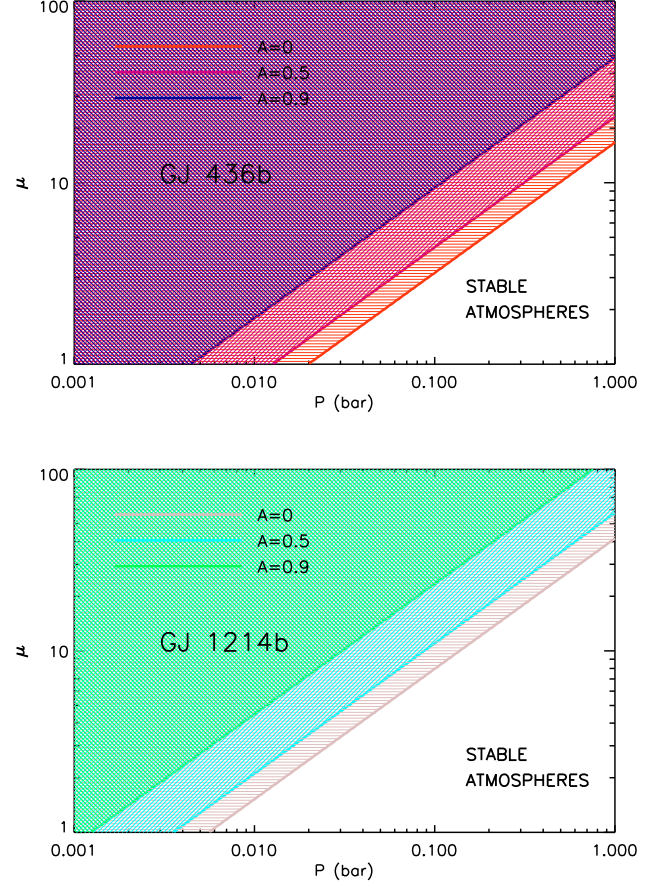


FIG. 4.— Stability diagrams in the parameter space of mean molecular weight (μ) versus infrared photospheric pressure (P), specialized to GJ 436b (top panel) and GJ 1214b (bottom panel). The hatched regions mark the regimes in which the atmosphere is unstable for a given value of the Bond albedo (\mathcal{A}). The stellar (M_* , R_* and T_*) and exoplanetary (R , a) parameters are all set to their observed values for each exoplanet (see text).

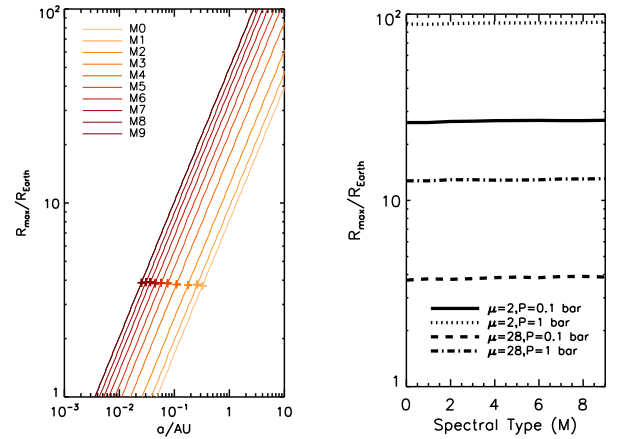


FIG. 5.— Maximum exoplanetary radius R_{max} allowed by the $t_{\text{adv}} < t_{\text{rad}}$ condition across the spectral types M0 to M9. The left panel shows the set of R_{max} curves, versus a , for $\mu = 28$ and $P = 0.1$ bar. The crosses mark the location of the center of the habitable zone for each spectral type. The right panel shows the R_{max} value corresponding to the center of each habitable zone as a function of the spectral type and for different combinations of the mean molecular weight μ and infrared photospheric pressure P .

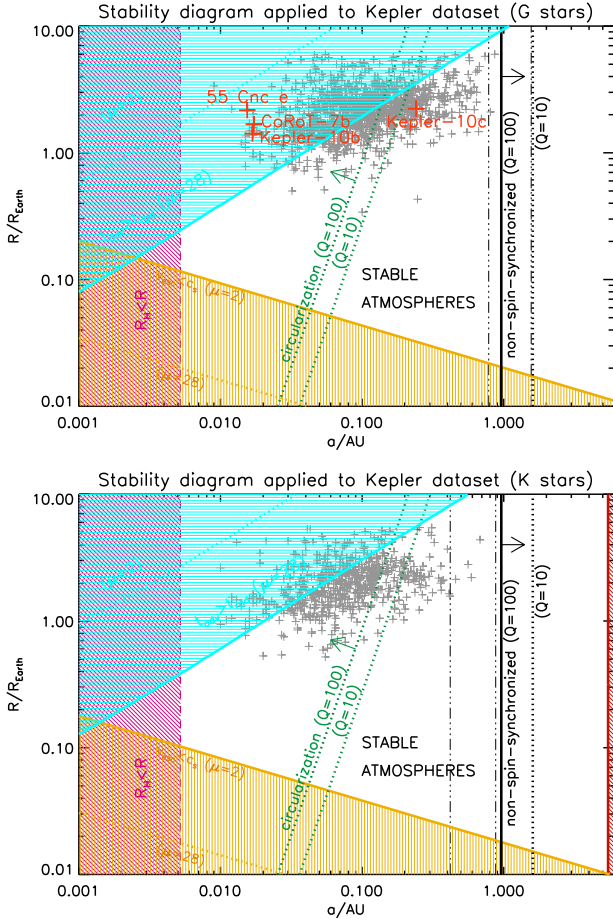


FIG. 6.— Basic stability diagrams applied to the *Kepler* dataset for G (top panel; 1135 objects) and K (bottom panel; 613 objects) stars. The atmospheric pressure is assumed to be $P = 1$ bar in these diagrams (see text). The triple-dot-dash lines denote the boundaries of the habitable zones. For the stability diagram applied to G stars, we include 55 Cancri e and CoRoT-7b as well as highlighting Kepler-10b and Kepler-10c. For the top panel, we have $a_{\text{con}} \approx 10$ and 136 AU for N_2 and H_2 , respectively; for the bottom panel, these values are about 5 and 71 AU.

they formed—remains an unconstrained exercise in some instances (e.g., Miguel et al. 2011). From this perspective, our analytical framework may be regarded as a survival—rather than formation—model, similar to what has been constructed for planetesimal disks (Heng & Tremaine 2010).

4.1. Caveats, Future work & Comparisons to Previous Work

We have assumed that when advection is inefficient, the nightside of a tidally-locked super Earth becomes arbitrarily cold. In reality, a non-negligible amount of heat may be advected to the nightside when $t_{\text{adv}} \sim t_{\text{rad}}$. The temperature difference between the dayside and the nightside is (Showman & Guillot 2002),

$$\Delta T \sim T_{\text{irr}} [1 - \exp(-t_{\text{adv}}/t_{\text{rad}})]. \quad (33)$$

Since $\Delta T \sim T_{\text{irr}} - T_{\text{night}}$, where T_{night} is the average temperature of the nightside hemisphere, we obtain

$$\frac{t_{\text{adv}}}{t_{\text{rad}}} \sim \ln \left[\frac{T_{\star}}{T_{\text{night}}} \left(\frac{R_{\star}}{a} \right)^{1/2} (1 - \mathcal{A})^{1/4} \right] \quad (34)$$

such that $t_{\text{adv}}/t_{\text{rad}} \rightarrow \infty$ when $T_{\text{night}} \rightarrow 0$; when $T_{\text{night}} \rightarrow T_{\text{irr}}$, we get $t_{\text{adv}}/t_{\text{rad}} \rightarrow 0$. Adopting $T_{\star} = 3240$ K, $R_{\star} = 0.203R_{\odot}$, $a = 0.001$ AU and $\mathcal{A} = 0$ yields $t_{\text{adv}} \sim 6t_{\text{rad}}$ if

$T_{\text{night}} = 10$ K. For $T_{\text{night}} = 100$ K, we get $t_{\text{adv}} \sim 3t_{\text{rad}}$. In other words, chemical species with low condensation temperatures (such as H_2 with $T_{\text{con}} \sim 10$ K) may remain in gaseous form even when the advective exceeds the radiative time scale by a factor of a few. Specifically, it is possible for a trickle of heat to maintain an atmosphere if it is hydrogen-dominated even in cases where $t_{\text{adv}} < t_{\text{rad}}$ is unfulfilled. Thus, the $t_{\text{adv}} < t_{\text{rad}}$ curve on the stability diagram should be viewed not as a sharp boundary, but a smooth transition. In general, chemical species with very low condensation temperatures probably do not require $t_{\text{adv}} < t_{\text{rad}}$ as a necessary condition for atmospheric stability. The gaseous state of these chemical species, with low condensation temperatures, may also be maintained by internal heat, which we do not consider.

Several other caveats provide motivation for future work. We have only considered atmospheres consisting of a single chemical species, but this approximation should not be too severe in situations where the given gas (e.g., H_2 , N_2) is the dominant constituent. More refined calculations may consider cocktails of greenhouse gases. Another assumption we have made is that our model, rocky exoplanets are not covered by oceans. Oceanic and atmospheric dynamics couple in a non-trivial manner, over a broad range of time scales, with consequences for the heat redistribution between the day- and nightside hemispheres, and are beyond the scope of the present study. Our hope is that our simple framework will motivate future work on a broad range of atmospheric constituents and not just Earth- or even Solar System-centric ones. More refined trains of thought include the consideration of feedback mechanisms such as the water ice-albedo feedback, which has been shown to operate weakly on tidally-locked exoplanets with Earth-like stellar irradiation and atmospheric conditions (Joshi, Haberle & Reynolds 1997; Joshi 2003).

Finally, we compare the present study to previous studies utilizing three-dimensional simulations of atmospheric circulation. For example, the rocky, CO_2 -dominated super Earth model considered by Wordsworth et al. (2011) has $t_{\text{rad}} \sim 10^7$ – 10^8 s, but they do not report their computed zonal wind speeds and thus we are unable to determine t_{adv} . However, we can infer from their Figure 1 that even though their model, in 1:1 tidal resonance, appears to have $t_{\text{adv}} \gtrsim t_{\text{rad}}$, the nightside temperatures are about 280–290 K. These temperatures lie above the condensation temperature of CO_2 at 20 bar, which is about 240 K, and thus atmospheric collapse does not occur. Joshi, Haberle & Reynolds (1997) do not provide the value of c_P used; if we use $c_P = 10^7$ erg K^{-1} g^{-1} , then we obtain $t_{\text{rad}} \sim 10^7$ s for their runs with $P \sim 1$ bar. Since $u_{\text{max}} \sim 10$ m s^{-1} , we have $t_{\text{adv}} \sim 10^5$ – 10^6 s ($< t_{\text{rad}}$) for their runs with $R = 6400$ and 13000 km, implying that these model atmospheres are mostly advective, which is consistent with the findings of Joshi, Haberle & Reynolds (1997).

4.2. Maximum Stability Radius

Our basic stability diagram (Figure 3) demonstrates that there is a maximum exoplanetary radius R_{max} above which the (thin) atmospheres of super Earths are unstable. In the left panel of Figure 5, we show R_{max} as a function of a across the spectral types M0 to M9. The less intensive irradiation from the cooler M stars leads to more lethargic radiative cooling in the atmospheres of their super Earths, which increases R_{max} across all values of a . However, this effect is offset by the center of the habitable zone moving inwards, towards the star, for later spectral types. The collective result is that R_{max} is insensitive to the spectral type. Rather, it is somewhat sensitive to

the mean molecular weight (μ) and the infrared photospheric pressure (P), as shown in the right panel of Figure 5. Atmospheres with lower photospheric pressures and higher mean molecular weights have lower values of R_{\max} , implying that the condition for stability is more stringent. For Earth-like atmospheres ($\mu = 28$) and $g \sim 10 \text{ m s}^{-2}$, the photospheres of super Earths with $R \sim 1\text{--}10R_{\oplus}$ need to be located at $P \gtrsim 0.1$ bar for stability.

4.3. Application to Kepler Exoplanets and Exoplanet Candidates

As a final demonstration of the power of our stability diagram, we apply it to the *Kepler* dataset (Borucki et al. 2011; Batalha et al. 2012). We include all exoplanets and exoplanet candidates with $R < 6R_{\oplus}$.⁸ We construct two diagrams for G ($5200 \text{ K} < T_{\star} \leq 6000 \text{ K}$) and K ($3700 \text{ K} < T_{\star} \leq 5200 \text{ K}$) stars using the average values of the stellar parameters for each sub-sample. We adopt $t_{\star} = 5$ Gyr for illustration, noting that this only affects the conditions on circularization and spin synchronization. In the absence of empirical constraints, we adopt Solar System-centric values for various parameters ($\rho_0 = 3 \text{ g cm}^{-3}$, $\mathcal{A} = 0.3$), but note that our estimates are insensitive to these assumptions. A key, unknown parameter is the infrared photospheric pressure. In Figure 6, we set $P = 1$ bar. With $P = 1$ bar, almost all of the 1135 *Kepler* exoplanets and exoplanetary candidates orbiting G stars have stable atmospheres if the atmospheres are dominated by molecular hydrogen ($\mu = 2$), whereas about 44% of them have stable atmospheres if they are Earth-like in composition ($\mu = 28$). For $P = 0.1$ bar, these percentages become about 88% and 1%, respectively.

We include in the stability diagram for G stars the measured R and a values for 55 Cancri e ($R \approx 2.17R_{\oplus}$, $a \approx 0.01544$ AU; Demory et al. 2011; Gillion et al. 2012) and CoRoT-7b ($R \approx 1.68R_{\oplus}$, $a \approx 0.0172$ AU; Léger et al. 2009). We also highlight the exoplanets Kepler-10b ($R \approx 1.416R_{\oplus}$, $a \approx 0.01684$ AU; Batalha et al. 2011) and Kepler-10c ($R \approx$

$2.227R_{\oplus}$, $a \approx 0.2407$ AU; Fressin et al. 2011). It remains possible that 55 Cancri e, CoRoT-7b and Kepler-10b may maintain minimal atmospheres—which do not extend beyond the day-night terminators and are dynamically dominated by vertical, rather than horizontal, flows—established through vapour saturation equilibrium with their continuously eroded rocky surfaces (Castan & Menou 2011; Valencia et al. 2011).

For the K stars (613 exoplanets and exoplanet candidates), we obtain similar numbers: for $P = 0.1$ bar, we get 97% ($\mu = 2$) and 4% ($\mu = 28$); for $P = 1$ bar, we get 100% ($\mu = 2$) and 70% ($\mu = 28$). Curiously, the exoplanet candidates and exoplanets residing within the habitable zones of both the *Kepler* G and K stars are likely to possess stable atmospheres, unlike the situation with M stars.

If these exoplanetary atmospheres are Earth-like ($P = 1$ bar, $\mu = 28$), then about half of them are expected to be stable. The continued expansion of the *Kepler* dataset and the eventual, inexorable pursuit of follow-up observations to further characterize these exoplanets will allow our predictions to be tested. For example, the photospheric infrared emission from atmosphere-less super Earths is likely to be emanated directly from their rocky surfaces, such that the dayside to nightside flux contrast will appear marked; these exoplanets will also exhibit flat transmission spectra. The scrutiny of atmosphere-less super Earths may provide a survey of their surface compositions (Hu, Ehlmann & Seager 2012).

KH acknowledges generous support by the Zwicky Prize Fellowship of ETH Zürich (Star and Planet Formation Group; PI: Michael Meyer). We are grateful to Sascha Quanz, George Lake and René Heller for illuminating conversations, as well as Jonathan Mitchell for stimulating comments which improved the clarity and quality of the manuscript. We thank the anonymous referee for a thoughtful report which improved the robustness of the study.

⁸ We remain agnostic about the *theoretical* demarcation between Earth- and Neptune-like exoplanets.

REFERENCES

- Anglada-Escudé, G., et al. 2012, ApJ Letters, in press (arXiv:1202.0446)
 Antuono, M. 2010, Journal of Fluid Mechanics, 658, 166
 Batalha, N.M., et al. 2011, ApJ, 729, 27
 Batalha, N.M., et al. 2012, preprint (arXiv:1202.5852)
 Bean, J.L., et al. 2011, ApJ, 743, 92
 Bodenheimer, P., Lin, D.N.C., & Mardling, R.A. 2001, ApJ, 548, 466
 Borucki, W.J., et al. 2011, ApJ, 736, 19
 Carter, J.A., Winn, J.N., Holman, M.J., Fabrycky, D., Berta, Z.K., Burke, C.J., & Nutzman, P. 2011, ApJ, 730, 82
 Castan, T., & Menou, K. 2011, ApJ, 743, L36
 Charbonneau, D. 2009, Proceedings of the IAU Symposium, eds. F. Pont, D. Sasselov & M. Holman, 253, pg. 1–8
 Charbonneau, D., et al. 2009, Nature, 462, 891
 Croll, B., Albert, L., Jayawardhana, R., Miller-Ricci Kempton, E., Fortney, J.J., Murray, N., & Neilson, H. 2011, ApJ, 731, L40
 de Mooij, E.J.W., et al. 2012, A&A, 538, A46
 Delfosse, X., et al. 2012, preprint (arXiv:1202.2467)
 Demory, B.-O., et al. 2011, A&A, 533, 114
 Désert, J.-M., et al. 2011, ApJ, 731, L40
 Ehrenreich, D., & Désert, J.-M. 2011, A&A, 529, A136
 Fressin, F., et al. 2011, ApJS, 197, 5
 Frierson, D.M.W., Held, I.M., & Zurita-Gotor, P. 2006, Journal of the Atmospheric Sciences, 63, 2548
 Garratt, J.R. 1994, Earth-Science Reviews, 37, 89
 Gill, A.E. 1980, Quarterly Journal of the Royal Meteorological Society, 106, 447
 Gillon, M., et al. 2012, A&A, 539, A28
 Goldreich, P., & Soter, S. 1966, Icarus, 5, 375
 Goody, R.M., & Yung, Y.L. 1989, Atmospheric radiation: theoretical basis, 2nd edition (New York: Oxford University Press)
 Held, I.M., & Suarez, M.J. 1994, Bulletin of the American Meteorological Society, 75, 1825
 Heller, R., Leconte, J., & Barnes, R. 2011, A&A, 528, A27
 Heng, K., & Spitkovsky, A. 2009, ApJ, 703, 1819
 Heng, K., & Tremaine, S. 2010, MNRAS, 401, 867
 Heng, K., Menou, K., & Phillipps, P.J. 2011, MNRAS, 413, 2380
 Heng, K., & Vogt, S.S. 2011, MNRAS, 415, 2145
 Heng, K., Frierson, D.M.W., & Phillipps, P.J. 2011, MNRAS, 418, 2669
 Heng, K., Hayek, W., Pont, F., & Sing, D.K. 2012, MNRAS, 420, 20
 Heng, K. 2012, ApJ, 748, L17
 Hu, R., Ehlmann, B.L., & Seager, S. 2012, ApJ, in press (arXiv:1204.1544)
 Joshi, M.M., Haberle, R.M., & Reynolds, R.T. 1997, Icarus, 129, 450
 Joshi, M. 2003, Astrobiology, 3, 415
 Kite, E.S., Gaidos, E., & Manga, M. 2011, ApJ, 743, 41
 Knopoff, L. 1964, Reviews of Geophysics, 2, 625
 Knutson, H.A., et al. 2011, ApJ, 735, 27
 Laughlin, G., Deming, D., Langton, J., Kasen, D., Vogt, S., Butler, P., Rivera, E., & Meschiarri, S. 2009, Nature, 457, 562
 Léger, A., et al. 2009, A&A, 506, 287
 Longuet-Higgins, M.S. 1968, Philosophical Transactions of the Royal Society of London, 262, 511

- MacDonald, A.E., Lee, J.L., & Xie, Y. 2000, *Journal of the Atmospheric Sciences*, 57, 2493
- Matsuno, T. 1966, *Journal of the Meteorological Society of Japan*, 44, 25
- Mayor, M., et al. 2009, *A&A*, 507, 487
- Menou, K. 2012, *ApJ*, 744, L16
- Merlis, T.M., & Schneider, T. 2010, *Journal of Advances in Modeling Earth Systems — Discussion (JAMES-D)*, 2, 13
- Miguel, Y., Kaltenecker, L., Fegley, B., & Schaefer, L. 2011, *ApJ*, 742, L19
- Miller-Ricci Kempton, E., Zahnle, K., & Fortney, J.J. 2012, *ApJ*, 745, 3
- Murray-Clay, R.A., Chiang, E.I., & Murray, N. 2009, *ApJ*, 693, 23
- Perna, R., Heng, K., & Pont, F. 2012, *ApJ*, in press (arXiv:1201.5391v2)
- Pierrehumbert, R.T. 2010, *Principles of Planetary Climate* (New York: Cambridge University Press)
- Pierrehumbert, R.T. 2011, *ApJ*, 726, L8
- Rogers, L.A., & Seager, S. 2010, *ApJ*, 716, 1208
- Selsis, F., Kasting, J.F., Levrard, B., Paillet, J., Ribas, I., & Delfosse, X. 2007, *A&A*, 476, 1373
- Showman, A.P., & Guillot, T. 2002, *A&A*, 385, 166
- Showman, A.P., & Polvani, L.M. 2010, *Geophysical Research Letters*, 37, L18811
- Showman, A.P., & Polvani, L.M. 2011, *ApJ*, 738, 71
- Tarter, J., et al. 2007, *Astrobiology*, 7, 30
- Troen, I.B., & Mahrt, L. 1986, *Boundary-Layer Meteorology*, 37, 129
- Wordsworth, R.D., Forget, F., Selsis, F., Millour, E., Charnay, B., & Madeleine, J.-B. 2011, *ApJ*, 733, L48
- Valencia, D., Ikoma, M., Guillot, T., & Nettelmann, N. 2011, *A&A*, 516, A20
- Vallis, G.K. 2006, *Atmospheric and Oceanic Fluid Dynamics: Fundamentals and Large-Scale Circulation* (New York: Cambridge University Press)
- Vogt, S.S., Butler, R.P., Rivera, E.J., Haghighipour, N., Henry, G.W., & Williamson, M.H. 2010, *ApJ*, 723, 954
- Yelle, R.V. 2004, *Icarus*, 170, 167